

# DOT tomography of the solar atmosphere

## VI. Magnetic elements as bright points in the blue wing of $H\alpha$ \*

J. Leenaarts<sup>1</sup>, R. J. Rutten<sup>1,2</sup>, P. Sütterlin<sup>1</sup>, M. Carlsson<sup>2,3</sup>, and H. Uitenbroek<sup>4</sup>

<sup>1</sup> Sterrekundig Instituut, Utrecht University, Postbus 80 000, 3508 TA Utrecht, The Netherlands  
e-mail: j.leenaarts@astro.uu.nl

<sup>2</sup> Institute of Theoretical Astrophysics, University of Oslo, PO Box 1029, Blindern, 0315 Oslo, Norway

<sup>3</sup> Center of Mathematics for Applications, University of Oslo, PO Box 1053, Blindern, 0316 Oslo, Norway

<sup>4</sup> NSO/Sacramento Peak, PO Box 62, Sunspot, NM 88349-0062, USA

Received 7 November 2005 / Accepted 17 December 2005

### ABSTRACT

High-resolution solar images taken in the blue wing of the Balmer  $H\alpha$  line with the Dutch Open Telescope show intergranular magnetic elements as strikingly bright features, similar to, but with appreciably larger contrast over the surrounding granulation than their more familiar manifestation as G-band bright points. Part of this prominent appearance is due to low granular contrast, without granule/lane brightness reversal as, e.g., in the wings of Ca II H & K. We use 1D and 2D radiative transfer modeling and 3D solar convection and magnetoconvection simulations to reproduce and explain the  $H\alpha$  wing images. We find that the blue  $H\alpha$  wing obeys near-LTE line formation. It appears particularly bright in magnetic elements through low temperature gradients. The granulation observed in the blue wing of  $H\alpha$  has low contrast because of the lack of  $H\alpha$  opacity in the upper photosphere, Doppler cancellation, and large opacity sensitivity to temperature working against source function sensitivity. We conclude that the blue  $H\alpha$  wing represents a promising proxy magnetometer to locate and track isolated intermittent magnetic elements, a better one than the G band and the wings of Ca II H & K although less sharp at given aperture.

**Key words.** Sun: magnetic fields – Sun: granulation – Sun: photosphere – Sun: chromosphere

### 1. Introduction

The Dutch Open Telescope (DOT) on La Palma was equipped with a tunable Lyot filter for the Balmer  $H\alpha$  line at 656.3 nm during the autumn of 2004. High-resolution images taken in the blue wing of  $H\alpha$  were found to display strikingly intense small-scale brightenings at the locations where intergranular magnetic elements cause the more familiar “G-band bright points” in the CH band around 430.5 nm. Figures 1 and 2 below show examples. Figure 3 demonstrates the potential of these  $H\alpha$  bright points for tracking intermittent magnetic elements over long durations. In this paper we reproduce and explain their formation using numerical simulations of various nature. We necessarily elaborate on the formation of the  $H\alpha$  wings in some detail.

G-band bright points<sup>1</sup> have been a major observational diagnostic of small magnetic elements in intergranular lanes in

the two decades following Muller & Roudier (1984). A brief review is given in the introduction to Paper IV of this series (de Wijn et al. 2005). The upshot is that G-band bright points remain a very useful proxy to chart small intergranular magnetic elements, be it not with strict one-to-one correspondence between brightness and magnetic flux density (cf. Berger & Title 2001; Berger et al. 2004), and that they derive their brightness primarily from deeper-than-outside radiation escape, sampling temperatures that are cooler than outside at equal geometrical height but hotter at equal optical depth. The latter excess is probably due to radiative hot-wall heating in the absence of convective heating, as proposed already by Spruit (1976). Magnetomechanical energy dissipation appears unimportant throughout the photosphere (Sheminova et al. 2005).

The G band provides the sharpest magnetic-element proxy imagery so far, in particular at the Swedish 1-m Solar Telescope (SST, see Wiehr et al. 2004; Berger et al. 2004; Ruppe van der Voort et al. 2005) and so remains the workhorse of high-resolution magnetic-element studies (e.g., Sánchez Almeida et al. 2004). Nevertheless, the G band is less

similar morphology at better resolution than the 0.3-arcsec diffraction limit of the 45-cm DOT at  $H\alpha$ .

\* Processed data and movie version of Fig. 1 are available in electronic form at <http://www.edpsciences.org>

<sup>1</sup> We use the traditional term “bright points” throughout this paper to designate features with sizes at about the angular resolution limit. Berger et al. (2004) used the 1-m SST to describe G-band features as “ribbons” and “flowers”. The  $H\alpha$  bright points are likely to show

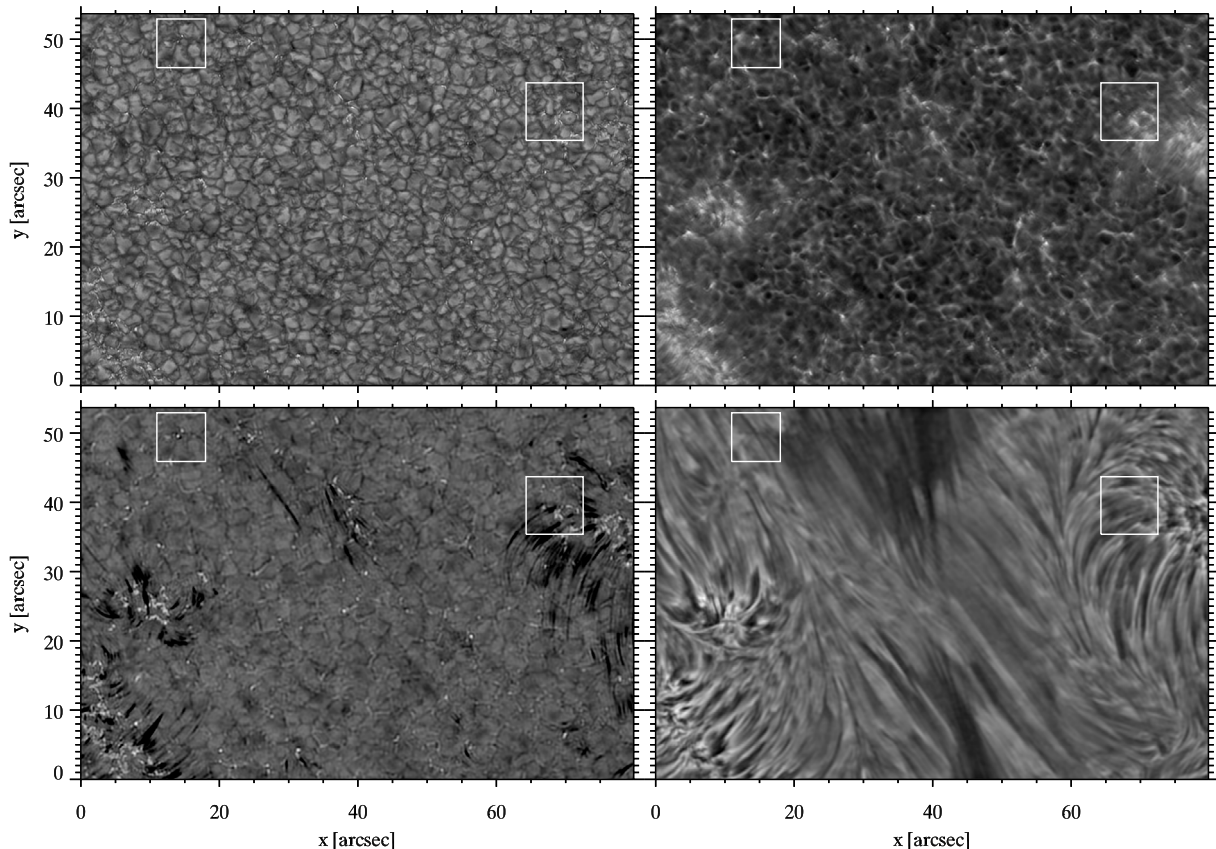


**Fig. 1.** DOT images of a quiet-Sun area below a quiescent filament. *Top left:* G band. *Top right:* Ca II H core. *Bottom left:* blue H $\alpha$  wing at  $\Delta\lambda = -0.08$  nm from line center. The lower greyscale limit is defined by dark mottle endings and is therefore clipped to restore the bright point visibility. *Bottom right:* H $\alpha$  line center. A gap in the filament lies at the center of the field. Axes:  $x$  = geocentric East-West,  $y$  = geocentric North-South, with arbitrary offsets. The first three images were taken simultaneously, the fourth 30 s earlier. The white rectangles outline small subfields used in Figs. 2 and 3. The lefthand one samples quiet network, the righthand one more active network.

suiting to track isolated magnetic elements with time than other diagnostics, in particular Ca II H & K and, as we show in this paper, the blue wing of H $\alpha$ .

The sketch in Fig. 8 of Rutten (1999) illustrates why Ca II H & K provide stabler magnetic-element proxies than the G band. Small intergranular magnetic structures vary much in cross-section and shape while being deformed by granular buffeting. In the LTE-formed G band they sometimes display bright hot walls, but only intermittently. G-band bright points may therefore transform, weaken, diffuse, or vanish while the magnetic flux itself is more stably present – although at varying concentration. Granular buffeting is indeed observed to act in this manner in the plage regions described by Rouppe van der Voort et al. (2005), breaking areas with high magnetic flux density such as G-band sheets (“ribbons”) into strings of bright points and deforming the “flowers” marking small flux concentrations.

In contrast, the H & K line cores display magnetic-element brightness more continuously, mainly through some as yet unidentified chromospheric magnetomechanical heating process that produces line-center emission peaks. They produce bright features in Ca II H & K filtergrams akin to above G-band bright points, at larger contrast with their surroundings but much less sharply (see Fig. 1 for examples). These

Ca II H & K bright points<sup>2</sup> tend to be present more consistently than the underlying photospheric G-band bright points. They are considerably less sharp because of resonance scattering within the solar atmosphere and through morphology change between photosphere and chromosphere, possibly including upward magnetic-element spreading as in idealized magnetostatic fluxtubes. They are therefore not easily resolved in crowded plage and network areas. However, in less crowded quiet-Sun network and especially in internetwork regions, Ca II H & K provide better diagnostics than the G band to track isolated magnetic elements with time. This property was used in Paper IV of this series by de Wijn et al. (2005) to establish the considerable longevity of internetwork field concentrations.

In this paper we show that H $\alpha$ -wing bright points provide even better recognizability (at given angular resolution) than Ca II H & K bright points, but through a different mechanism. They derive high contrast primarily from specific H $\alpha$  line formation properties within the photosphere. In Sect. 2 we display pertinent observations. In Sect. 3 we first use 2D radiative

<sup>2</sup> The magnetic ones, not K<sub>2V</sub> or H<sub>2V</sub> acoustic internetwork grains which are not studied here. The latter cannot be distinguished from magnetic internetwork bright points unless followed in time. The acoustic ones then stand out through three-minute modulation and the magnetic ones through longevity (e.g., Fig. 2 of Rutten et al. 2004a).

transfer modeling in a 3D MHD simulation snapshot slice to model photospheric  $H\alpha$  wing formation in magnetic elements. Additional 1D modeling using a standard solar model atmosphere is added to explain some  $H\alpha$  properties. We then use the full 3D snapshot of the MHD simulation to compare computed with observed magnetic-element brightness contrast in the blue  $H\alpha$  wing.

## 2. Observations

The data used here were obtained with the Dutch Open Telescope (Rutten et al. 2004b) on La Palma on October 6, 2004 during campaign JOP178. The target was the gap in a quiescent filament seen in the bottom-right panel of Fig. 1, at solar coordinates S16 E11. Polarimetry of this region with THEMIS<sup>3</sup> shows that the clusters of magnetic elements at left and right in the field of view had opposite polarity. A tomographic multi-wavelength image sequence was recorded during excellent seeing from 08:47 UT until 09:42 UT with the DOT's multi-wavelength speckle imaging system (Bettonvil et al. 2003). The latter had just been extended with the Lyot filter for  $H\alpha$  previously used at the Ottawa River Solar Observatory (Gaizauskas 1976). It transmits a tunable band of 0.025 nm FWHM. Between the successive speckle bursts it was switched sequentially between  $H\alpha$  line center and the blue  $H\alpha$  wing at  $\Delta\lambda = -0.08$  nm. These wavelength settings were made precise through an initial imaging scan through the whole profile. The four other DOT cameras registered the same field in the G band, blue continuum, red continuum, and Ca II H line center (pass-band 0.128 nm). The burst cadence was 30 s at 100 frames/burst with five-camera synchronization.

The speckle-masking reconstruction and other reduction steps are summarized in Rutten et al. (2004b). The resulting image sequences were spatially aligned and corrected for remaining quality variations by equalization of the average radial power spectrum<sup>4</sup>.

Figure 1 shows sample images covering the full field of view. The first panel shows the familiar G-band scene of granulation with intergranular clusters of tiny bright points which mark magnetic elements. The second panel shows the same scene in the core of Ca II H. The filter is wide enough to include part of the inner wings which show the reversed granulation analyzed in Papers II and III of this series (Rutten et al. 2004a; Leenaarts & Wedemeyer-Böhm 2005). It appears as a bright mesh pattern on which acoustic  $H_{2V}$  grains are superimposed. The magnetic elements causing G-band bright points appear quite bright in Ca II H but very unsharp, with bright aureoles of diffuse emission around them.

The third panel of Fig. 1 shows the same scene in the blue wing of  $H\alpha$ , the fourth panel does so in  $H\alpha$  line center. The filament is prominent in the latter but transparent in the  $H\alpha$  wing. The dark streaks in the blue-wing image are part of the elongated  $H\alpha$  mottles seen at line center. The latter do not connect

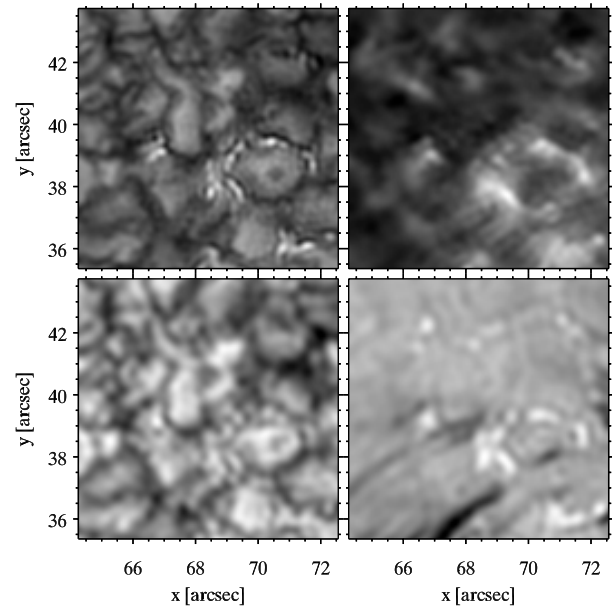


**Fig. 2.** Cut-out image magnifications corresponding to the righthand rectangle in Fig. 1. The four images were taken simultaneously. *Top left:* G band. *Top right:* Ca II H line center. *Bottom left:* near- $H\alpha$  red continuum at 650.0 nm. *Bottom right:* blue  $H\alpha$  wing. Notice the bright point at  $(x, y) = (66.7, 42.2)$  in  $H\alpha$ , which barely shows up in the G band and is not present in Ca II H.

the two regions of opposite polarity across the filament gap, but curve away avoiding the neutral line marked by the filament. Some mottle endings are likely to appear extra dark in the blue-wing image through Doppler blueshift.

Apart from the dark mottle endings, the  $H\alpha$  blue-wing image shows a greyish background of non-reversed granulation at low contrast, plus strikingly bright points. In the network areas these are concentrated into clusters from which the dark mottle endings emanate. The Ca II H image also shows bright point but less sharp and (as we show below) with different morphology. It also shows short streaks emanating from these. The  $H\alpha$  line center also shows bright points near the mottle endings, but with yet larger difference in morphology. The chromospheric features in these images are discussed further in Rutten (2006).

The G-band image serves to identify all  $H\alpha$ -wing bright points as G-band bright points. They are sharper in the G band but stand out much clearer in the  $H\alpha$  wing. Comparison of the four images immediately establishes  $H\alpha$ -wing bright points as excellent magnetic-element markers, less sharp but much brighter than their G-band counterparts while much sharper than their Ca II H counterparts.

Figure 2 shows a similar comparison for the righthand subfield outlined in Fig. 1, at large magnification. The G-band subfield in the upper-left panel shows strings of bright points marking magnetic flux in the lower-right part of the panel. They are sharp but have rather low contrast compared with their surroundings. Their sizes are close enough to the resolution limit that they are apt to vanish through cancellation against the surrounding intergranular darkness when diminishing in size or brightness (Title & Berger 1996).

<sup>3</sup> <http://bass2000.bagn.obs-mip.fr/jop178/oct6/oct6.html>

<sup>4</sup> The processed data and a movie version of Fig. 1 are available at <http://dot.astro.uu.nl> and at <http://www.edpsciences.org>

The upper-right Ca II H panel shows enhanced emission at the site of G-band bright points, but diffuse and not one-to-one. The reverse granulation in the remainder of the image also represents a vague rather than a one-to-one contrast reversal.

The red continuum image at the lower left has appreciably lower resolution and lower contrast than the G-band image due to the increase of diffraction with wavelength, smaller Planck function sensitivity to temperature, and lack of magnetic-element brightness enhancement as occurs in the G band. Some granules are appreciably brighter than the brightest magnetic elements.

For  $H\alpha$  one might expect similar loss of bright-point visibility as in the neighboring red continuum, or lack of spatial matching as in Ca II H. However, the lower-right panel of Fig. 2 showing the same subfield in the blue  $H\alpha$ -wing displays all bright points seen in the G-band image at larger contrast. In particular, the bright point at  $(x, y) = (66.7, 42.2)$  stands out only in  $H\alpha$ . All other structures in  $H\alpha$  that are as bright or brighter match the morphology of G-band bright points closely, although less sharply. In the lower-right part of the subfield they make up the strings of bright beads called “filigree” by Dunn & Zirker (1973). These authors also proposed to call the individual elements “crinkles” in view of their appearance – conform this image, but resolved into G-band bright points in the upper-left image, and those are likely to resolve at yet higher resolution into the flowers and ribbons of Berger et al. (2004) and Rouppe van der Voort et al. (2005). The background contrast in the  $H\alpha$  wing, consisting of normal rather than reversed granulation, is exceptionally small except where dark mottle endings occur.

The upper-right part of the  $H\alpha$ -wing image in Fig. 2 also shows a long chain of less bright beads in a dark lane. The G-band displays only greyish small-scale structure there. Sometimes such structure represents speckle reconstruction artifacts caused by DOT camera defects. However, inspection of the temporal evolution of this area shows that the brighter beads in the chain possess, while migrating around, longevities of well over ten minutes. These indicate magnetic nature.

The large  $H\alpha$  brightness of G-band bright points, the low contrast of the granular background in  $H\alpha$ , and the above indication that  $H\alpha$  is a sensitive magnetic-feature finder suggest that the  $H\alpha$  wing is an even better indicator to locate and follow long-lived isolated magnetic elements than Ca II H & K. Figure 3 confirms this expectation. The G-band time slice shows only intermittent bright-point presence. The wiggles are probably small co-registration errors. Instead, both the  $H\alpha$  wing and the Ca II H core show much clearer brightness streaks betraying long-duration magnetic presence. Of these two,  $H\alpha$  is the better proxy for locating and tracking such magnetic elements. The lefthand bright point in the  $H\alpha$  image is not identifiable as a magnetic element in the other two images, but the  $H\alpha$  time slice clearly marks it as one. A few minutes later it merges with the righthand one by migration in  $x$ . The joint trail ends later when the feature migrated in  $y$  off the cut location, but it actually existed until the end of the image sequence.

The surroundings of the  $H\alpha$  streak roughly reflect the granulation seen in the G-band panel but at lower contrast. The Ca II H time-slice background is instead dominated by

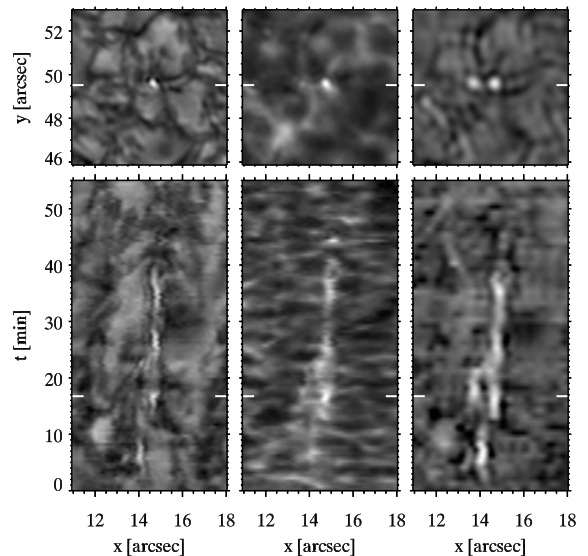


**Fig. 3.** Cut-out image magnifications and time slices corresponding to the lefthand outline sampling quiet network in Fig. 1, from left to right for the G band, Ca II H, and the  $H\alpha$  wing. *Top row:* subfield images. The lefthand one of the two  $H\alpha$  bright points is less evident at the other wavelengths. The white ticks indicate the horizontal cut along which the temporal evolution is shown below. *Bottom row:*  $x-t$  time slices. The white ticks indicate the time sampled by the images above, which is 9 min after the full-field samples in Fig. 1.

three-minute acoustic oscillations superimposed on reversed granulation. The bright point at  $t = 45$  min is likely an acoustic grain.

### 3. Simulations

In order to explain the high visibility of magnetic elements in the blue wing of  $H\alpha$  we use a single time-step snapshot of a three-dimensional (3D) magneto-hydrodynamics simulation by Stein & Nordlund with a code incorporating an LTE equation of state including partial ionization and multi-group LTE radiative transfer (Stein & Nordlund 1998). The same snapshot was used by Carlsson et al. (2004) to analyse G-band bright point formation towards the solar limb.

The extent of the simulation is 6 Mm in both horizontal directions and from  $-2.5$  Mm below  $\langle\tau_{500}\rangle = 1$  to 0.5 Mm above it. The horizontal resolution is 23.6 km. The vertical resolution varies from 35 km in the lower layers to 15 km in the upper layers. The simulation was started with a homogeneous vertical magnetic field of 250 G.

We evaluated the emergent intensity in the  $H\alpha$  wing that originates from this snapshot using the RH code of Uitenbroek (2001) to compute radiative transfer in the snapshot in a variety of ways. It permits LTE or NLTE radiative transfer modeling in 2D or 3D geometry with partial or complete frequency redistribution. We used it here to perform  $H\alpha$  modeling both in 2D admitting departures from LTE and in 3D assuming LTE. We also present 1D results using the FAL-C model of Fontenla et al. (1993) for explanatory purposes.

In the 2D NLTE modeling we took a 2D slice from the snapshot, reducing the horizontal resolution by a factor of two

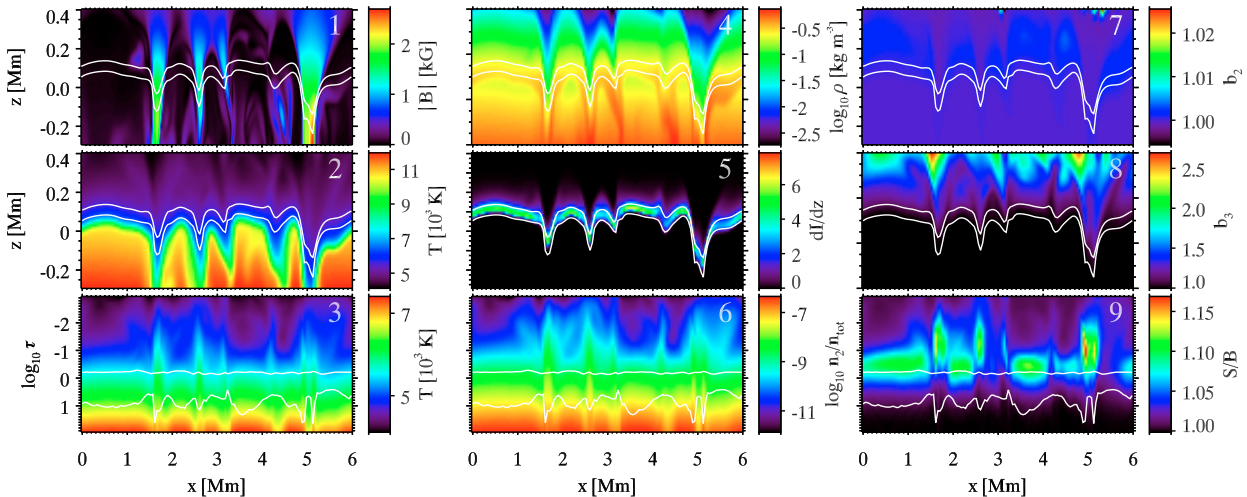


**Fig. 4.** NLTE H $\alpha$  wing formation in a vertical  $x$ - $z$  slice through the MHD simulation. The first two columns illustrate H $\alpha$  bright point formation. The third column quantifies departures from LTE. The color scales are specified per panel in the bars to the right. The first and second rows show vertical stratifications on the common geometrical height scale ( $z$  axis). The bottom row shows individual stratifications against the logarithm of the radial optical depth along each column for  $\Delta\lambda = -0.08$  nm from line center. The superimposed curves specify the mean height of formation for the intensity at  $\Delta\lambda = -0.08$  nm from line center (upper curve) and in the background continuum at H $\alpha$  (lower curve). *Panel 1:* absolute value of the magnetic field strength. *Panels 2 and 3:* temperature against height and optical depth. Note the difference in temperature range. *Panel 4:* logarithm of the gas density against height. *Panel 5:* intensity contribution  $dI/dz$  at  $\Delta\lambda = -0.08$  nm from line center. Units:  $10^{-13}$  J m $^{-3}$  s $^{-1}$  Hz $^{-1}$  sr $^{-1}$ . *Panel 6:* logarithm of the population density of the lower level of H $\alpha$  as a fraction of the total hydrogen density; *Panels 7 and 8:* NLTE population departure coefficients for the lower and upper levels of H $\alpha$ . *Panel 9:* ratio of the H $\alpha$  source function  $S$  and the Planck function  $B$  against optical depth.

to increase the numerical stability of the radiative transfer computations. We added the upper part of the FAL-C model to its top. This results in a 2D atmosphere slice of 127 points in  $x$  and 135 points in  $z$ , with a horizontal extent of 6000 km and extending from  $-450$  km below to  $2150$  km above  $\tau_{500} = 1$ . We used a 5-level-plus-continuum hydrogen atom to compute NLTE radiative transfer with partial frequency redistribution (PRD) through this model atmosphere in the H $\alpha$  line, with 3 ray angles per octant. Inspection showed that PRD effects are only important above 500 km, well above the formation height of the H $\alpha$  wing and therefore negligible for the discussion here. We then adopted complete frequency redistribution (CRD) to compute a NLTE solution with 10 rays per octant. The latter increase is needed to account for the large horizontal variations in the lower atmosphere.

The results of the 2D NLTE modeling (shown in Fig. 4 and discussed below) demonstrated that departures from LTE are small for the formation of the H $\alpha$  intensity at  $\Delta\lambda = -0.08$  nm. This permitted us to perform 3D modeling with the complete snapshot assuming LTE, a feasible computing task. For this modeling we used the full 3D simulation snapshot without adding a chromosphere on top. In both the 2D and the 3D modeling we took Dopplershifts from the flow velocities into account in the line profile computation. We used a Voigt profile for the H $\alpha$  line. In the damping wings it represents an approximation for the actual Holtmark distribution.

### 3.1. Bright points in the 2D NLTE simulation

Figure 4 shows details of the formation of H $\alpha$  wing bright points as computed from the 2D NLTE simulation. The

first panel shows the absolute value of the vector magnetic field throughout the vertical slice. It contains three fluxtube-like magnetic elements with kilogauss field strength, one weaker-field one near  $x = 3.2$  Mm, and a subsurface magnetic concentration at  $x = 4.5$  Mm. Panel 2 shows the temperature against height. All magnetic elements display marked isotherm dips: they are appreciably cooler inside than outside at the heights of interest. The latter are specified by the superimposed curves marking the mean height of formation along columns for the H $\alpha$  wing and its background continuum. The upper curve corresponds to the vertical line-wing intensity contribution functions shown in panel 5 and represents these very well. Both curves dip deeply within the magnetic elements due to low gas density (panel 4) where magnetic pressure is appreciable.

The bottom row panels display various quantities not versus geometrical height but as a function of the radial optical depth in the H $\alpha$  wing, a format introduced by Carlsson et al. (2004) which displays atmospheric stratifications “as seen” by the vertically emergent radiation. The two mean height of formation curves change correspondingly. The upper one becomes virtually flat near  $\tau = 1$ . The lower one displays large spatial variations in its offset from the upper one, as set by the  $n_2$  lower level population (panel 6) with low population producing small separation. Panel 3 is strikingly different from panel 2 by showing large upward isotherm humps instead of dips at the magnetic element locations. The difference between the two representations results primarily from the substantial variations in vertical gas density stratification between columns. These are shown in panel 4. Comparison of panels 4 and 5 shows that the upward tails of the H $\alpha$ -wing contribution functions decay appreciably faster than the density stratifications, making the contribution

functions unusually narrow in vertical extent. This is discussed further in Sect. 3.2. Panel 6 shows the fractional hydrogen population occupying the  $n = 2$  lower level of H $\alpha$  on columnar optical depth scales. It is remarkably similar to panel 3 because the high excitation energy of this level makes its population very sensitive to the temperature (also discussed further in Sect. 3.2).

Panels 1 to 6 illustrate the formation mechanism of the H $\alpha$ -wing bright points. It is similar to G-band bright point formation. The relatively low gas density in magnetic elements (panel 4) results in appreciable Wilson depressions in the mean height of formation (panel 5 and the superimposed curves). Although the magnetic-element insides are cooler than their surroundings at any geometrical height (panel 2), panel 3 shows that they already have higher temperature at  $\tau = 1$  compared with the surrounding granules. This lateral temperature excess increases towards smaller  $\tau$  thanks to flatter  $dT/d\tau$  temperature gradients (panel 3). Its weighting into the outer tail of the intensity contribution functions causes enhanced brightness in magnetic elements.

The flatter  $dT/d\tau$  temperature gradients within magnetic elements also cause flatter  $dn_2/d\tau$  population gradients (panel 6). One would expect correspondingly higher formation and loss of brightness contrast, but the sensitivity of collisional H $\alpha$  broadening to the gas density compensates for these increases. The low density inside magnetic elements reduces the broadening and with it the relative amount of line extinction in the damping wings, increasing the Wilson depression between outside and inside sampling. A test computation assuming height-independent wing shape of an artificial line with similar height of formation indeed gave a decrease of 5–10% in the emergent intensity within the magnetic elements.

The remaining panels in the third column of Fig. 4 serve to evaluate the importance of departures from LTE in H $\alpha$  wing formation. Panels 7 and 8 show NLTE population departure coefficients for the  $n = 2$  and  $n = 3$  lower and upper levels of H $\alpha$ . The lower-level values are everywhere near unity demonstrating that the line opacity obeys LTE very closely.

The upper-level populations (panel 8) virtually equal the LTE value up to the upper height of formation curve. Higher up this level becomes appreciably overpopulated, probably due to radiative overionization in the Balmer continuum causing closure recombination into the  $n = 3$  level (cf. explanation in Rutten & Carlsson 1994). This overpopulation results in slight  $S > B$  source function excess within the magnetic elements and above the granules, as shown in panel 9. The largest  $S/B$  excesses occur at smaller optical depth for the magnetic elements than for the granules.

Figure 5 shows the H $\alpha$  wing intensities that result from 2D radiative transfer computation for the simulation slice of Fig. 4. The upper panel is for monochromatic computation at  $\Delta\lambda = -0.08$  nm. The solid curve represents the computed NLTE intensities, the grey curves LTE intensities. The latter are everywhere smaller than the NLTE values, but only marginally. The differences are largest for granules, in which the  $S/B$  excesses in panel 9 of Fig. 4 occur at larger optical depth than in the magnetic elements. However, they remain far smaller than the variations due to the magnetic elements.

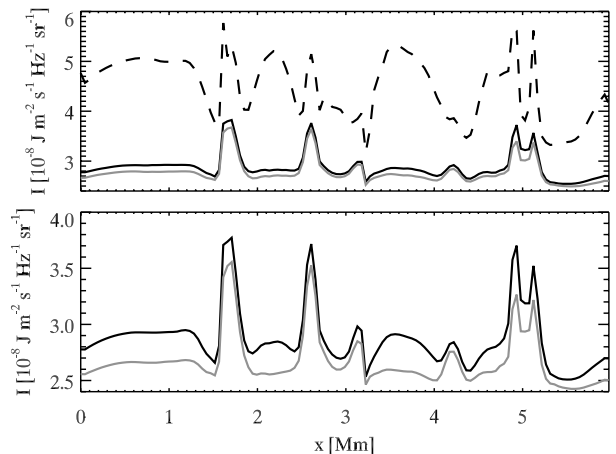


**Fig. 5.** H $\alpha$  wing intensity computed from the 2D simulation in Fig. 4. Black solid curves: NLTE. Grey curves: LTE. *Top:* monochromatic intensity at  $\Delta\lambda = -0.08$  nm from line center. The dashed higher-value curve is for the background continuum intensity at H $\alpha$ . *Bottom:* computed intensity with spectral integration over the DOT H $\alpha$  passband.

The dashed curve in the upper panel of Fig. 5 shows the emergent continuum intensity. Its shape is roughly the reverse of the  $\tau_{\text{cont}} = 1$  curve in Fig. 4. The magnetic elements are at most slightly brighter than the granules, in good agreement with the red continuum image in Fig. 2. The H $\alpha$  intensities are appreciably lower everywhere, but much more so within granules: in H $\alpha$  the magnetic elements gain large excess brightness. Comparison with panel 1 of Fig. 4 shows that all strong-field magnetic elements stand out through marked H $\alpha$ -wing intensity increase.

The lower panel of Fig. 5 shows the computed NLTE and LTE intensities after spectral integration over the DOT H $\alpha$  filter passband. It shows similar behavior as the monochromatic intensities in the upper panel. Thus, the simulation produces H $\alpha$  wing bright points at least qualitatively comparable to our observations. On average, the spectrally integrated NLTE intensity is 7% brighter than for LTE due to the  $S/B$  excesses shown in Fig. 4. The relative brightness increase from LTE to NLTE is generally larger within the granules since their  $S/B$  excesses peak at larger optical depth (panel 9 of Fig. 4). It is also larger within granules than for the monochromatic case (upper panel) because addition of intensity closer to line center implies contribution from higher layers, for which the corresponding mean contribution curve in panel 9 of Fig. 4 cuts closer through the granular  $S/B$  peaks.

### 3.2. Absence of reversed granulation

Solar images taken in the wings of Ca II H & K show reversed granulation, a pattern comparable to the granulation seen in the continuum but with reversed brightness modulation. It is also seen in the center panel of Fig. 1 due to the width of the DOT Ca II H filter. It is primarily caused by convection flow reversals occurring between 0.2 Mm and 0.6 Mm above continuum optical depth unity (Rutten et al. 2004a; Leenaarts & Wedemeyer-Böhm 2005).

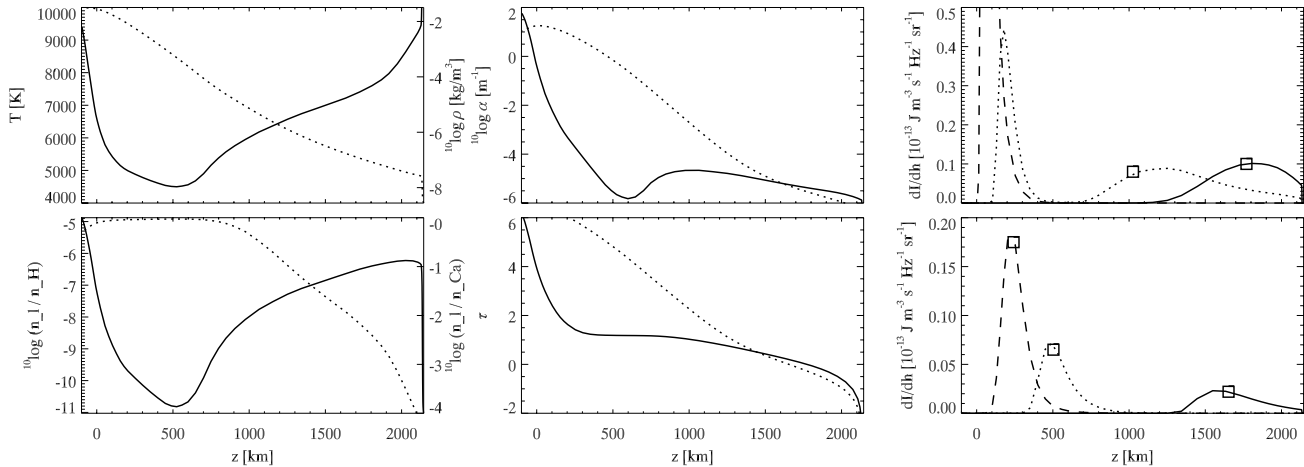


**Fig. 6.** Illustration explaining the difference between H $\alpha$  and Ca II H wing formation. *Top left:* FALC temperature (lefthand scale, solid) and density (righthand scale, dotted). *Bottom left:* number density of the lower level of the line relative to the total number density of the atomic species, respectively for H $\alpha$  (lefthand scale, solid) and for Ca II H (righthand scale, dotted). *Top center:* line center extinction coefficient for H $\alpha$  (solid) and Ca II H (dotted). *Bottom center:* line center optical depth for H $\alpha$  (solid) and Ca II H (dotted). *Top right:* intensity contribution function for  $\Delta\lambda = 0$  (solid),  $-0.038$  (dotted), and  $-0.084$  nm (dashed) from line center in H $\alpha$ . Squares indicate the  $\tau = 1$  height. *Bottom right:* the same for Ca II H, at  $\Delta\lambda = 0$  (solid),  $-0.024$  (dotted), and  $-0.116$  nm (dashed) from line center.

In contrast, our H $\alpha$  wing images show no reversed granulation (Fig. 1). The explanation is that the large excitation energy (10.2 eV) of the  $n = 2$  lower level causes large temperature sensitivity of the line opacity. In Boltzmann equilibrium the relative temperature sensitivity of the population density  $n$  of a level with excitation energy  $\Delta E$  and partition function  $Z$  is  $(dn/dT)/n = \Delta E/kT^2 - (1/Z) dZ/dT$ . The population sensitivity to temperature therefore scales with the excitation energy, since  $Z$  varies only slightly with temperature. Figure 6 illustrates the profound effect of this large sensitivity by comparing the formation of Ca II H and H $\alpha$  in the FALC model of Fontenla et al. (1993). Its temperature and density stratifications are shown in the first panel. The lower-left panel shows the fractional population  $n_l/n_{\text{element}}$  of the lower level of each line. Due to its temperature sensitivity the hydrogen  $n = 2$  population drops dramatically around the temperature minimum. In contrast, the lower level of Ca II H is almost insensitive to temperature through being the ground state of the dominant calcium ionization stage. Only at chromospheric levels occurs depopulation through Ca II ionization to Ca III.

The two center panels show the striking resulting H $\alpha$ –Ca II H differences in line-center extinction  $\alpha$  and optical depth  $\tau$ . Neglecting stimulated emission, the first reflects the product of gas density (first panel) and fractional population; the second the buildup of its inward integration. The H $\alpha$  extinction shows a pronounced minimum at the temperature minimum which produces a nearly flat plateau in its optical depth buildup around  $z = 500$  km. In contrast, Ca II H has almost linear dependence between extinction and density and regular optical depth buildup.

The lack of optical depth buildup around the temperature minimum for H $\alpha$  translates into a lack of intensity contribution since the term  $d \ln \tau / dz$  vanishes in the decomposition

$$I = \int_0^\infty S e^{-\tau} d\tau = \int_0^\infty S \tau e^{-\tau} \frac{d \ln \tau}{dz} dz \quad (1)$$

introduced by Carlsson & Stein (1994, 1997). This lack of buildup explains the large difference in atmospheric sampling by the H $\alpha$  and Ca II H wings shown by contribution functions in the rightmost panels of Fig. 6. The dotted curve for the inner wing of H $\alpha$  in the upper panel is doubly peaked, with an extended gap in the temperature minimum region (cf. Schoolman 1972). By judicious wavelength choice one might shift the  $\tau = 1$  location marked by a rectangle to the temperature minimum at  $h \approx 500$  km, but the source function at  $\tau = 1$  would not be at all representative for the emergent intensity. The latter would instead sense and mix the conditions in the two peaks, much lower and much higher in the atmosphere. When tuning the sampling wavelength from line center out through the blue or red wing of H $\alpha$  one suddenly drops in sensitivity from the high chromosphere to the low photosphere.

In contrast, the Ca II H & K wings represent excellent diagnostics to scan smoothly through the whole photosphere by tuning the passband (lower rightmost panel of Fig. 6). The inner wings sampled by the DOT Ca II H filter originate in upper-photosphere layers where convection reversal causes reversed granulation. The H $\alpha$  wing misses these layers altogether. However, the outer H $\alpha$  wing provides relatively narrow contribution functions to sample the low photosphere.

### 3.3. Small granulation contrast

Our blue-wing H $\alpha$  images (e.g., the one in Fig. 1) show granulation but at very low contrast due to multiple reasons. First: at red wavelengths the Planck function temperature sensitivity is smaller than in the G band. Second: the wider point spread function due to increased diffraction decreases the small-scale contrast. Third: the granular velocity-intensity correlation contributes Doppler cancellation of the contrast in blueward line wings. Intergranular downflows Doppler-shift the blue wing redward through the filter passband so that intergranular

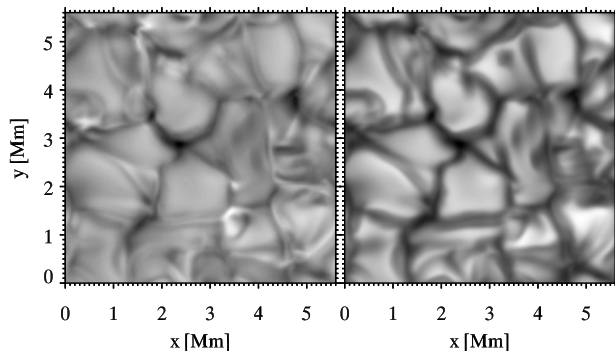


**Fig. 7.** Demonstration of the H $\alpha$  opacity sensitivity to temperature with a hydrodynamic granulation simulation. *Left:* emergent intensity in the blue H $\alpha$  wing. The rms intensity variation is 0.047. *Right:* emergent intensity in the wing of a fake H $\alpha$  line at only 1 eV excitation. The rms intensity variation is 0.144, much larger than at left.

darkening is compensated by deeper-down higher-temperature sampling. Similarly, granular upflows shift a deeper part of the line into the blue-wing passband and so offset granular brightening by higher-up lower-temperature sampling. This compensation works best in lines with steep wings, for example the Ba II 455.4 nm line illustrated in Fig. 6 of Sütterlin et al. (2001), and so has much larger effect in the H $\alpha$  wings than in the extended wings of H & K (where it reverses sign with the granulation).

A fourth effect elaborated here is decreased brightness response to temperature due to the large H $\alpha$  opacity sensitivity to temperature. Spectral features that are formed in LTE without such sensitivity, such as the wings of Ca II H & K, brighten through source function increase where or when the temperature in the line-forming region increases. For high-excitation lines the opacity increase produced by temperature increase leads to higher-up line formation. When the temperature decreases outward, as is normally the case in the photosphere, the higher-up sampling implies darkening which offsets the local source function increase. A cartoon illustration of this compensation is given in Fig. 4 of Leenaarts et al. (2005). A model illustration is given here in Fig. 7. It compares LTE intensities in the H $\alpha$  wing computed from a granulation simulation with those computed using a fake H $\alpha$  line having the same opacity but with its lower level at only 1 eV instead of 10.2 eV. The snapshot was taken from the radiation-hydrodynamics granulation simulation by Wedemeyer et al. (2004). The rms intensity variation in the lefthand granulation scene is much smaller than at right.

### 3.4. Bright points in the 3D LTE simulation

Our finding in Sect. 3.1 that LTE formation is a good assumption for the H $\alpha$  wing in the photosphere allows us to compute emergent wing intensities from the full 3D MHD simulation snapshot. The results are shown in Fig. 8.

The first panel shows the emergent intensity in the H $\alpha$  wing after spectral application of the DOT filter transmission. The top right panel shows the magnetic field strength at the surface.

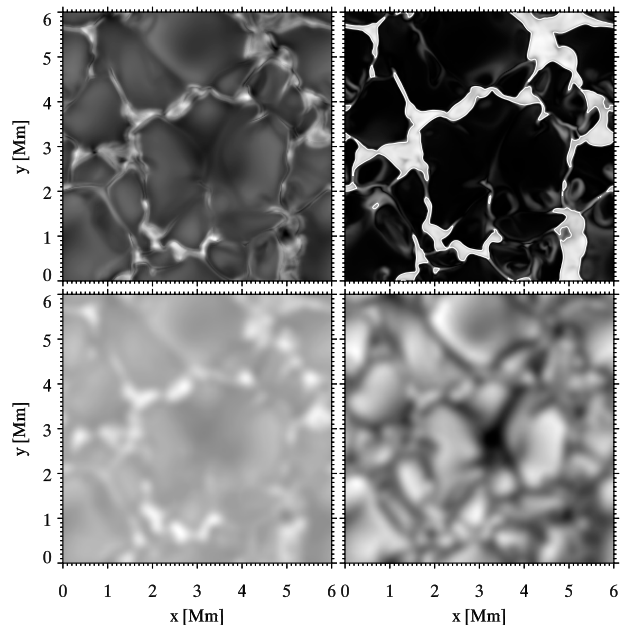


**Fig. 8.** Results from the 3D MHD simulation. *Top left:* computed intensity in the H $\alpha$  wing. *Top right:* magnitude of the vector magnetic field at  $\tau_{500} = 1$ . The grey scale ranges from 2 G to nearly 2 kG. The white contours are at 1 kG. *Bottom left:* simulated DOT H $\alpha$  wing image, obtained by convoluting the computed intensity pattern with the Airy point-spread function corresponding to 45-cm aperture diameter. The grey scale was set to the same range as the H $\alpha$  image in Fig. 2. *Bottom right:* similar simulated DOT image but for the continuum at 650 nm and grey-scaled to its dynamic range.

The brightest features in the computed H $\alpha$  scene correspond to magnetic field strengths above 1 kG.

The lower panels show the simulated H $\alpha$  wing and red continuum scenes convolved with a point spread function corresponding to the DOT diameter of 45 cm. In addition, for the artificial H $\alpha$  image the brightness scale was clipped to cover similar range as the real DOT H $\alpha$  image in Fig. 2. It looks much like the latter, showing low-contrast granulation, barely visible intergranular lanes, and magnetic elements in chains of roundish brightness enhancements. The artificial red-continuum image in the lower-right panel shows the same morphology but with the magnetic elements about as bright as the granules, also in good agreement with the corresponding DOT image in Fig. 2.

Figure 9 compares observed and computed H $\alpha$  profiles and brightness contrasts, with spatial separation of bright points and granulation. Emergent-intensity H $\alpha$  profiles were computed along each column of the 3D simulation assuming LTE. The spatial separation was obtained by applying a brightness mask to the artificial H $\alpha$  wing image at lower left in Fig. 8, labeling every pixel that has  $I/\langle I \rangle \geq 1.12$  as belonging to a bright point, and defining all other pixels to represent granulation. This threshold is the  $3\sigma$  level of the rms intensity variation in all H $\alpha$  wing images in our DOT sequence.

The upper panel of Fig. 9 shows emergent H $\alpha$  profiles spatially averaged over the whole simulation snapshot and spatially averaged over the magnetic elements alone. For comparison, the solar disk-center profile from the NSO Fourier

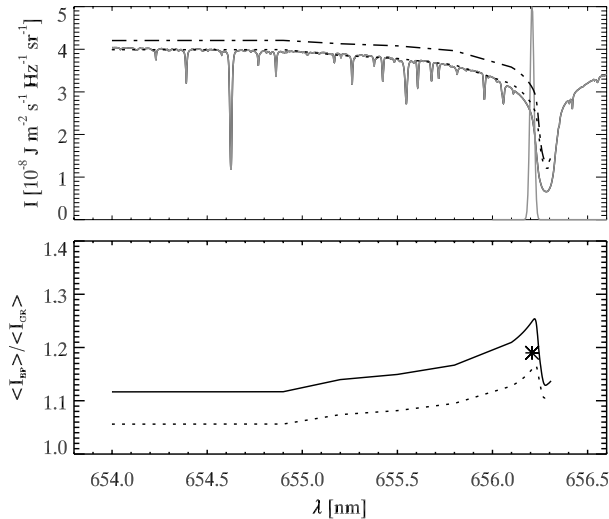


**Fig. 9.** *Top:* H $\alpha$  spectra. Solid grey: solar atlas profile. Dotted: spatially averaged spectrum from the 3D LTE simulation. Dash-dotted: average bright-point spectrum from the simulation. The narrow Gaussian shows the location and shape of the H $\alpha$  filter passband used in our H $\alpha$  wing observations. *Bottom:* average bright-point intensity divided by the average granule intensity, versus wavelength. Solid: un-smearing simulation. Dotted: simulation after convolution with the DOT-diameter Airy function. The asterisk specifies the observed contrast.

Transform Spectrometer atlas produced by J.W. Brault and calibrated by Neckel & Labs (1984) is overlaid. The graph shows excellent agreement between the NSO atlas and the simulated full-field average along the extended blue wing. However, in the inner wing the simulation produces slightly higher intensity, contrary to the expected NLTE correction indicated by Fig. 5. This excess is not caused by the relatively large number of bright points in the simulation since the profile that results from spatial averaging over the granules alone differs only marginally from the full-field average. We suspect that the computed inner-wing excess is due to the neglect of dark structures in the high layers sampled by the outer H $\alpha$  formation peak that are not accounted for in the 3D simulation. H $\alpha$  line-center movies, including the one sampled in Fig. 1, indicate that the upper peak samples low-intensity chromospheric mottles and fibrils nearly everywhere, often with large Dopplershifts. Some of these contribute considerable darkness in the blue wing, especially near network (Fig. 1).

The dash-dotted upper curve in the upper panel of Fig. 9 holds for the spatial average over the computed bright points. Note that it is appreciably higher than the full-field average throughout the whole line profile, even though the magnetic elements in Fig. 4 are at all heights cooler than their surroundings at equal geometrical height and the 3D simulation has no chromosphere. This once again illustrates that excess brightness originating in the upper photosphere does not necessarily imply magnetomechanical heating (cf. the similar conclusion from Ca II H spectrometry in Sheminova et al. 2005).

The lower panel of Fig. 9 shows two curves specifying the ratio of the average bright point intensity to the average granule intensity against wavelength, one for the full-resolution

simulation scene (upper curve) and one for the DOT-like spatially smeared simulation scene. The latter has lower contrast, as expected. The sharp drop in the contrast curves lies slightly to the red of 656.2 nm where the corresponding  $\tau = 1$  height jumps abruptly from the deep photosphere to higher layers (Fig. 6). In the simulation these have small lateral temperature variation. In reality,  $\tau = 1$  lies in the mottled chromosphere where LTE computation and the simulation are certainly invalid.

Finally, we compare the average brightness of the H $\alpha$  bright points in the observations with the simulation curves. Applying the brightness mask to the observed image sequence and to the smeared passband-integrated H $\alpha$  wing simulation delivers  $\langle I_{bp} \rangle / \langle I_{FOV} \rangle = 1.19$  for the observations and  $\langle I_{bp} \rangle / \langle I_{FOV} \rangle = 1.15$  for the simulation. The observed value is shown by the asterisk in Fig. 9 and indeed lies above the peak in the dotted simulation curve. Thus, the LTE simulation produces smaller bright point contrast than is actually observed. The differences between the NLTE and LTE curves in the lower panel of Fig. 5 indicate that departures from LTE reduce the computed contrast and so increase the discrepancy. In addition, proper accounting for the broad scattering wings of the point-spread function which are not present in our Airy-function simulation smearing is likely to increase the discrepancy further.

#### 4. Discussion

As noted above we are not the first to describe bright points in the wing of H $\alpha$ . The often reprinted “filigree” image from the Sacramento Peak Vacuum Tower Telescope in Fig. 1 of Dunn & Zirker (1973) has an H $\alpha$  panel at  $\Delta\lambda = -7/8 \text{ \AA}$  that shows them particularly well. But it was a surprise how much promise they possess as a diagnostic to locate intermittent magnetic elements and track these with time (Fig. 3). They are less sharp than G-band bright points but they show the same morphology with much better contrast over their surroundings. On the other hand, they are sharper than Ca II H & K line-center bright points, and they do not suffer from the contamination by reversed granulation that affects the H & K wings nor from bright-point morphology change as in the H & K cores (Fig. 2).

Similarly to G-band bright points which are exceptionally bright through the addition of CH opacity and from partial CH destruction in magnetic elements (Carlsson et al. 2004), H $\alpha$ -wing bright points are exceptionally bright through the addition of Balmer-line opacity and the reduction of collisional damping in magnetic elements. The particular flatness of the granular background pattern in the blue H $\alpha$  wing derives from Doppler cancellation and large lower-level excitation energy (Figs. 6 and 7).

Our 3D LTE simulation reproduces the H $\alpha$  wing bright points quite well (Fig. 8) but does not fully match their average brightness contrast (Fig. 9). Our 2D NLTE simulation indicates that departures from LTE worsen this discrepancy (Fig. 5). An obvious speculation is to attribute the deficit to absence of chromospheric heating in our modeling. The Ca II H & K lines display similarly raised wings from photospheric Wilson-depression sampling of magnetic elements that are cooler than their surroundings, but they also display

high emission peaks in their line cores above magnetic elements that must be attributed to magnetomechanical heating (cf. Sheminova et al. 2005). The H $\alpha$  case differs. A chromospheric component would likely be formed at similar height as the Ca II H & K peaks, in fact with less contribution from the upper photosphere (Fig. 6). For such chromospheric formation the spatial morphology would differ because magnetic elements are not ramrod straight. However, the H $\alpha$  bright-point morphology in Fig. 2 tracks the G-band morphology closely, whereas the Ca II H bright point morphology differs appreciably. This difference indicates that H $\alpha$  bright points at  $\Delta\lambda = -0.08$  nm from line center are predominantly photospheric. Closer to line center they are likely to be obscured by overlying chromospheric structures. The bright points at the mottle foots in the line-center image in Fig. 1 indeed differ yet more from the G-band bright point morphology than the Ca II H bright points (cf. Rutten 2006).

Are their other spectral features that may be similarly useful? In principle one searches for considerable photospheric line opacity which partially vanishes in low-density fluxtubes through e.g., atomic ionization, molecular dissociation, or profile narrowing in damping wings. The Mg I b<sub>1</sub> wing was presented already by Beckers (1976) as a good filigree diagnostic. High excitation helps by flattening the granular background contrast, as explained in Fig. 6. Steep line wings (on the blue side) additionally loose granular contrast through Doppler cancellation, as in Ba II 455.4 nm (Sütterlin et al. 2001). The CN band shortward of 388.34 nm was presented as a promising alternative to the G band by Rutten et al. (2001) and more recently by Zakharov et al. (2005). However, the latter's specification implies that their passband hardly reached the CN bandhead and was dominated instead by the blue wing of H $\zeta$  (upper level  $n = 8$ ) plus some Fe I lines. Their reported bright-point contrast was therefore not due to CN, but may be due to H $\zeta$  wing formation akin to H $\alpha$  wing formation. The same point is made in the recent study of Uitenbroek & Tritschler (2005) who used the same snapshot of the MHD simulation used here to predict bright point brightnesses in the CN band. They conclude that the CN contrast is unlikely to be markedly better than in the G band.

We suggest that another promising spectral feature is the blue wing of H $\beta$  at 486.1 nm. It should produce bright points in similar fashion to H $\alpha$  while offering larger Planck function contrast and sharper imaging from smaller diffraction. The Irkutsk Lyot filter described by Sütterlin et al. (2001) can be tuned to H $\beta$  and is being installed on the DOT. We aim to present simulated H $\beta$  bright-point formation in another paper.

*Acknowledgements.* We are deeply indebted to V. Gaizauskas concerning the H $\alpha$  filter. Its installation on the DOT involved the Instrumentele Groep Fysica of Utrecht University. We thank the referee for improvements to the paper. The DOT is operated by Utrecht University at the Spanish Observatorio del Roque de los Muchachos of the Instituto de Astrofísica de Canarias and is presently funded by the Department of Physics and Astronomy of Utrecht University, the Netherlands Organisation for Scientific Research NWO, the Netherlands Graduate School for Astronomy NOVA, and SOZOU. The DOT efforts and the Utrecht-Oslo collaboration are part

of the European Solar Magnetism Network funded by the EC under contract HPRN-CT-2002-00313. This research made much use of NASA's Astrophysics Data System literature server.

## References

- Beckers, J. M. 1976, in *Physics of Solar Planetary Environments*, 89
- Berger, T. E., Rouppe van der Voort, L. H. M., Löfdahl, M. G., et al. 2004, *A&A*, 428, 613
- Berger, T. E., & Title, A. M. 2001, *ApJ*, 553, 449
- Bettonvil, F. C., Suetterlin, P., Hammerschlag, R. H., Jagers, A. P., & Rutten, R. J. 2003, in *Innovative Telescopes and Instrumentation for Solar Astrophysics*, ed. S. L. Keil, & S. V. Avakyan, *Proc. SPIE*, 4853, 306
- Carlsson, M., & Stein, R. F. 1994, in *Chromospheric Dynamics*, 47
- Carlsson, M., & Stein, R. F. 1997, *ApJ*, 481, 500
- Carlsson, M., Stein, R. F., Nordlund, Å., & Scharmer, G. B. 2004, *ApJ*, 610, L137
- de Wijn, A. G., Rutten, R. J., Haverkamp, E. M. W. P., & Sütterlin, P. 2005, *A&A*, 441, 1183
- Dunn, R. B., & Zirker, J. B. 1973, *Sol. Phys.*, 33, 281
- Fontenla, J. M., Avrett, E. H., & Loeser, R. 1993, *ApJ*, 406, 319
- Gaizauskas, V. 1976, *JRAS Can.*, 70, 1
- Leenaarts, J., Sütterlin, P., Rutten, R. J., Carlsson, M., & Uitenbroek, H. 2005, in *ESA SP-596: Chromospheric and Coronal Magnetic Fields*, 15
- Leenaarts, J., & Wedemeyer-Böhm, S. 2005, *A&A*, 431, 687
- Muller, R., & Roudier, T. 1984, *Sol. Phys.*, 94, 33
- Neckel, H., & Labs, D. 1984, *Sol. Phys.*, 90, 205
- Rouppe van der Voort, L. H. M., Hansteen, V. H., Carlsson, M., et al. 2005, *A&A*, 435, 327
- Rutten, R. J. 1999, in *Third Advances in Solar Physics Euroconference: Magnetic Fields and Oscillations*, *ASP Conf. Ser.*, 184, 181
- Rutten, R. J. 2006, in *Solar MHD: Theory and Observations*, ed. J. Leibacher, H. Uitenbroek, & R. F. Stein, *Procs. 23rd NSO workshop*, *ASP Conf. Ser.*, in press
- Rutten, R. J., & Carlsson, M. 1994, in *Infrared Solar Physics*, *IAU Symp.*, 154, 309
- Rutten, R. J., de Wijn, A. G., & Sütterlin, P. 2004a, *A&A*, 416, 333
- Rutten, R. J., Hammerschlag, R. H., Bettonvil, F. C. M., Sütterlin, P., & de Wijn, A. G. 2004b, *A&A*, 413, 1183
- Rutten, R. J., Kiselman, D., Rouppe van der Voort, L., & Plez, B. 2001, in *Advanced Solar Polarimetry – Theory, Observation, and Instrumentation*, *ASP Conf. Ser.*, 236, 445
- Sánchez Almeida, J., Márquez, I., Bonet, J. A., Domínguez Cerdeña, I., & Muller, R. 2004, *ApJ*, 609, L91
- Schoolman, S. A. 1972, *Sol. Phys.*, 22, 344
- Sheminova, V. A., Rutten, R. J., & Rouppe van der Voort, L. H. M. 2005, *A&A*, 437, 1069
- Spruit, H. C. 1976, *Sol. Phys.*, 50, 269
- Stein, R. F., & Nordlund, A. 1998, *ApJ*, 499, 914
- Sütterlin, P., Rutten, R. J., & Skomorovsky, V. I. 2001, *A&A*, 378, 251
- Title, A. M., & Berger, T. E. 1996, *ApJ*, 463, 797
- Uitenbroek, H. 2001, *ApJ*, 557, 389
- Uitenbroek, H., & Tritschler, A. 2005, *ApJ*, in press
- Wedemeyer, S., Freytag, B., Steffen, M., Ludwig, H.-G., & Holweger, H. 2004, *A&A*, 414, 1121
- Wiehr, E., Bovelet, B., & Hirzberger, J. 2004, *A&A*, 422, L63
- Zakharov, V., Gandorfer, A., Solanki, S. K., & Löfdahl, M. 2005, *A&A*, 437, L43